Continental Shelf Research 29 (2009) 728–740

Contents lists available at ScienceDirect

Continental Shelf Research

journal homepage: www.elsevier.com/locate/csr

Interaction of a river plume with coastal upwelling in the northeastern South China Sea

Jianping Gan [a,*], Li Li [b], Dongxiao Wang [c], Xiaogang Guo [b]

[a] Department of Mathematics and the Atmospheric Marine and Coastal Environment Program, Hong Kong University of Science and Technology, Clear Water Bay, Kowloon, Hong Kong, China
[b] The Third Institute of Oceanography, State Oceanic Administration, Xiamen, China
[c] LED, South China Sea Institute of Oceanography, Chinese Academy of Sciences, Guangzhou, China

ARTICLE INFO

Article history:
Received 12 April 2008
Received in revised form
3 November 2008
Accepted 2 December 2008
Available online 9 December 2008

Keywords:
Coastal upwelling
River plume
Buoyancy forcing

ABSTRACT

Observational and modeling studies were conducted to investigate the Pearl River plume and its interaction with the southwesterly driven upwelling circulation in the northern South China Sea during the summer. After exiting the Pearl River Estuary, the discharged freshwater generates a nearly stationary bulge of freshwater near the entrance of the estuary. Forced by the wind-driven coastal upwelling current, the freshwater in the outer part of the bulge flows downstream at the speed of the current and forms a widening and deepening buoyant plume over the shelf. The plume axis gradually shifts offshore of the current maximum as a result of currents induced by the contrasting density at the nose of plume and by the intensified Ekman drift in the plume. In this plume–current system, the fraction of the discharged freshwater volume accumulated in the bulge reaches a steady state and the volume of newly discharged freshwater is transported downstream by the upwelling current. Enhancement of stratification by the plume thins the surface frictional layer and enhances the cross-shelf circulation in the upper water column such that the surface Ekman current and compensating flow beneath the plume are amplified while the shoaling of the deeper dense water in the upwelling region changes minimally. The pressure gradient generated between the buoyant plume and ambient seawater accelerates the wind-driven current along the inshore edge of the plume but retards it along the offshore edge. Along the plume, downward momentum advection is strong near the highly nonlinear source region and a weaker upward momentum advection occurs in the far field over the shelf. Typically, the plume is shaped by the current over the shelf while the current itself is adjusting to a new dynamic balance invoked by the plume-induced changes of vertical viscosity and the horizontal pressure gradient. The spatial variation of this new balance leads to a coherent change in the cross-isobath transport in the upper water column during upwelling.

1. Introduction

Discharge from a river or from an estuary can form a buoyant and nutrient-rich freshwater plume in the sea. Such a plume generally yields a right-tilted (in the northern hemisphere) bulge of buoyant freshwater at the entrance to the estuary (e.g. Chao, 1986). However, with the existence of wind-driven currents in the ambient coastal water, the fate and characteristics of the plume, as well as the currents, are controlled by the interaction between the plume and wind-driven circulation (e.g. Hickey et al., 1998; Berdeal et al., 2002; Fong and Geyer, 2002). The plume insulates surface coastal water from the water below and amplifies the efficiency of wind forcing near the surface (Lentz, 2001). At the same time, the lateral density gradient or pressure gradient formed between the buoyant plume and ambient seawater geostrophically alters the intensity of the wind-driven currents (e.g. Chao, 1988; Rennie et al., 1999). The interaction between the river plume and the coastal current is an important dynamic process that governs nearshore circulation along many coasts around the world. This study investigates the three-dimensional response of cross-shelf transport in upwelling to the interactive dynamic forcing in the coupled plume-circulation environment in the northern South China Sea (NSCS, Fig. 1).

The Pearl River is the third largest river in China. It discharges on the northern coast of the South China Sea at an average annual discharge rate of about 10,000 $m^3 s^{-1}$ with a maximum of more than 25,000 $m^3 s^{-1}$ in the wet season (June to August). After leaving the Pearl River Estuary (PRE), the buoyant Pearl River water, with its high terrestrial nutrient concentration, spreads over a broad continental shelf in the NSCS (Figs. 1 and 2). During

* Corresponding author. Tel.: +852 2358 7421.
E-mail address: magan@ust.hk (J. Gan).

0278-4343/$ - see front matter © 2008 Elsevier Ltd. All rights reserved.
doi:10.1016/j.csr.2008.12.002

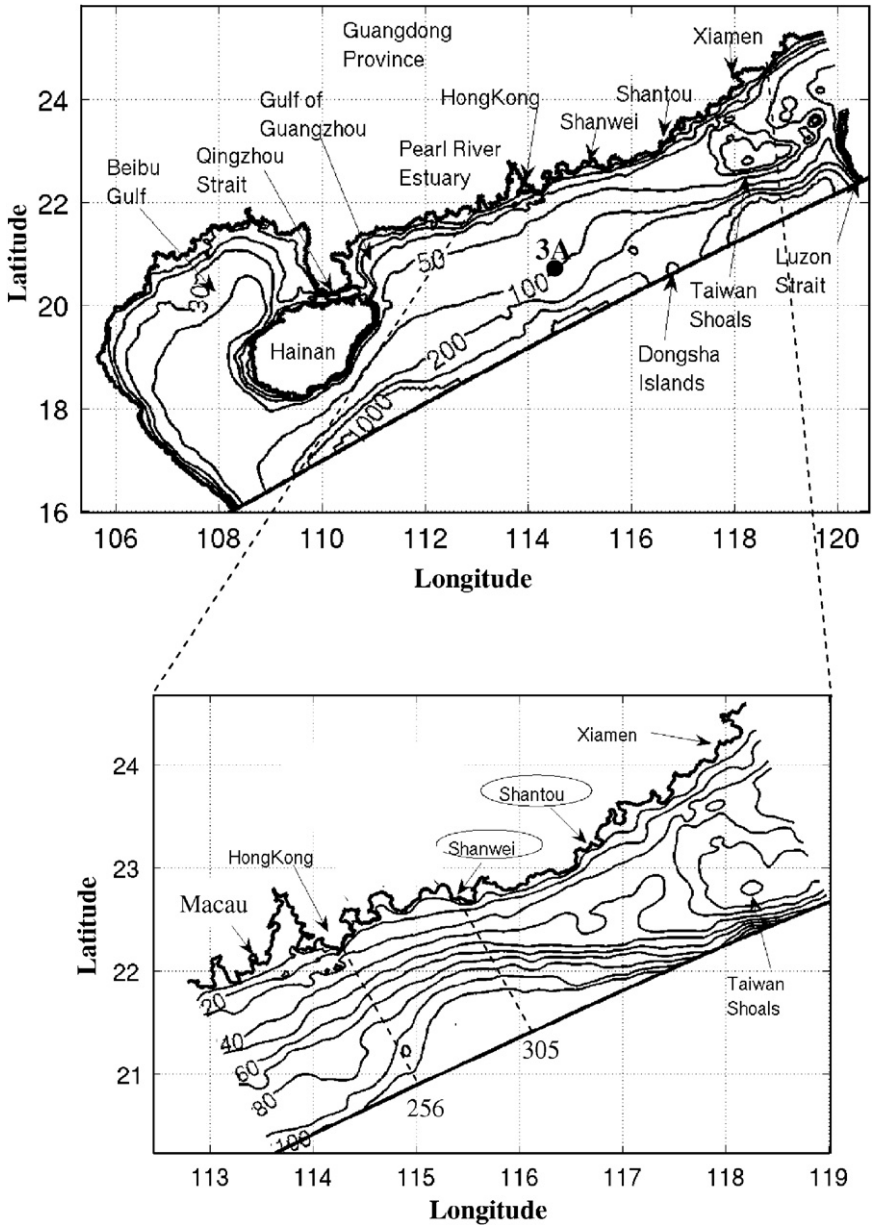

Fig. 1. The topography (in meters) in the northern South China Sea and an enlargement of the area between Macau and Xiamen. Two selected cross-shelf sections (dashed lines), at Hong Kong and Shanwei, are marked by their grid numbers. Station 3A is marked by a solid dot.

the wet season, the coastal ocean over the continental shelf of the NSCS is dominated by the southwesterly driven upwelling (Shaw, 1992; Li, 1993; Su, 1998). Gan et al. (2007) found that the wind-induced currents during upwelling are mainly directed eastward or southeastward over the shelf east of the PRE, following the local shelf topography. As a result, the plume detaches itself from the coast and the bottom and a high concentration of chlorophyll travels southeastward (Fig. 2). Previous studies of the Pearl River plume concentrated their efforts on processes within or around the PRE (Dong et al., 2004; Wong et al., 2004). The response of the plume to the upwelling current and the modulation of upwelling circulation by the buoyant plume have not been investigated over the NSCS shelf.

The interaction between a river plume and ambient currents has been extensively explored in many studies, either by numerical modeling or by field investigations. Chao and Boicourt (1986) found that a surface-trapped plume moves offshore and becomes thinner during upwelling favorable winds, whereas the plume attaches to the coast and forms an additional downwind coastal jet which elongates, accelerates, and deepens the plume during downwelling favorable winds. Hickey et al. (1991) found that an anomalously strong pulse of river water accounted for 10–20% of the variance in the current about 50 km downstream of the river. The response of a plume to variable river discharge was later discussed by Yankovsky et al. (2001). Munchow and Garvine (1993a) identified dynamically distinct regions of high along-shelf nonlinearity in the source region near the estuary and linear dynamics further downstream. Munchow and Garvine (1993b) found that during upwelling wind spreads buoyant water offshore while dense water underneath the buoyant water moves toward the coast. Oey and Mellor (1993) and Kourafalou et al. (1996a) suggested that variability of plume associated with instability plays an important role in shelf circulation. Yankovsky and Chapman (1997) discussed the characteristics of seaward movement in a surface and bottom-advected plume based on a cyclostrophic balance subject to rotational effects. Hickey et al.

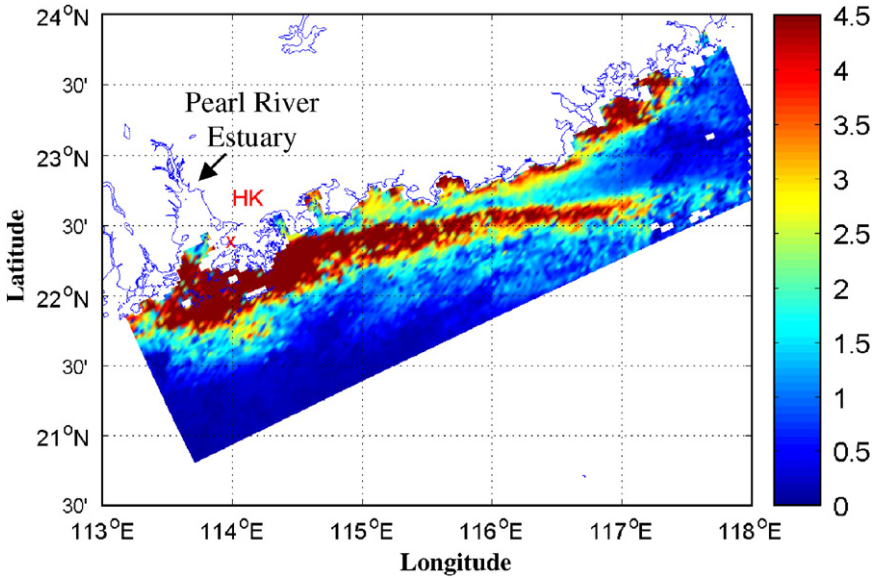

Fig. 2. Time average of MODIS surface chlorophyll (mgm^{-3}) resulting from Pearl River discharge and coastal upwelling that have been forced with a combination of northeastward and shoreward winds from June 29 to July 7, 2003.

(1998) found that the plume is driven mainly by wind-driven Ekman surface currents and that along-shelf buoyancy-driven currents and wind-driven currents are comparable in magnitude 20 km from a river mouth. Rennie et al. (1999) found that the current in the nose of a plume has the properties of an internal gravity current under rotation and that the coastal current velocities inshore of a plume were two to three times faster than the ambient shelf flow. Interaction between river plumes and wind-driven coastal ambient currents were also presented by Berdeal et al. (2002) and Whitney and Garvine (2005). A recent field measurement by Chant et al. (2008) and a modeling study by Fong and Geyer (2002) pointed out that wind or ambient current is required in order for the entire volume discharged by a river to be transported downstream. Using satellite-captured Synthetic Aperture Radar (SAR) and repeated field measurements, Nash and Moum (2005) detected the Columbia River plume (Oregon, USA) flowing as gravity waves into the coastal ocean, causing horizontal convergence and internal waves in the plume front. A recent study of Changjiang diluted water (Chen et al., 2008) showed the formation of a baroclinically unstable front and eddies as well as their interactions with currents in the East China Sea.

Unlike studies of plumes themselves, the response of the three-dimensional wind-driven cross-shelf transport in coastal upwelling to the plume over the shelf has not received much attention. However, Allen et al. (1995) and Lentz (2001), reported that the wind-driven coastal current is profoundly influenced by the stratification in the water column. With the increase of vertical stratification by the plume, the mixed layer thins and the role of wind stress in the surface Ekman layer is enhanced. As a result, the intensity of surface alongshore currents and cross-shelf circulation is amplified while the coastal wind-driven jet is located farther from shore. This study reports the extended investigation of the upwelling presented in Gan et al. (2007) by focussing on the dynamics of the interaction between the buoyant plume and the three-dimensional wind-driven transport in coastal upwelling. We will first discuss the characteristics of the plume, upwelling circulation, and their interactions as observed in field measurements from the NSCS (Section 2). Results obtained from a three-dimensional modeling study will be presented to kinematically identify the invoked processes (Section 3) and to dynamically illustrate the interactive forcing mechanism between the plume and upwelling circulation (Section 4).

2. Observational study

Hydrographic data collected in the NSCS during the upwelling season in July–August of 2000 and 2002 are shown in Figs. 3–5. Measurements were recorded along five CTD (conductivity–temperature–depth) transects over the northern part of the shelf in 2000 (Zhuang et al., 2005). Eight transects covering the region from the PRE to east of the Taiwan Shoals were conducted in 2002 (Xu et al., 2003). The corresponding wind stress averaged over the sampling periods is also displayed in Fig. 3. Wind stress data were obtained from QuickScat.

2.1. The plume and its responses to upwelling currents

Upwelling driven by the strong southwest monsoon during the 2000 cruise (Fig. 3) formed relatively high sea surface salinity (SSS) over the inner shelf along the coast of NSCS. The highest SSS (>34 psu) was located off Shantou because of the local intensification of upwelling in the lee of the coastal cape (Gan et al., 2007; Gan and Allen, 2002). With a Pearl River discharge rate of 10,300 $m^3 s^{-1}$during this period, a surface buoyant plume was propelled eastward from the PRE by the wind-driven upwelling jet. The plume was patchy with the lowest salinity located near the PRE and over the mid-shelf off Shanwei.

During the 2002 cruise, the upwelling-favorable southwest wind was relatively weak and it gradually decreased to the east of Shantou (Fig. 3). However, the river discharge rate of 16,100 $m^3 s^{-1}$ was 56 percent larger than that of 2001. Consequently, a much stronger buoyant plume spread from the PRE to 118°E in the alongshore direction and spanned from 80 to 100 km cross-shore. A bulge of plume water was formed near the entrance of the PRE. A fraction of the plume water emanated from the outer part of the bulge and advected southeastward due to the upwelling coastal current. The plume water subsequently bifurcated as it approached the Taiwan Shallows (Fig. 1) and flowed through the northern and southern parts of the Taiwan Shoals.

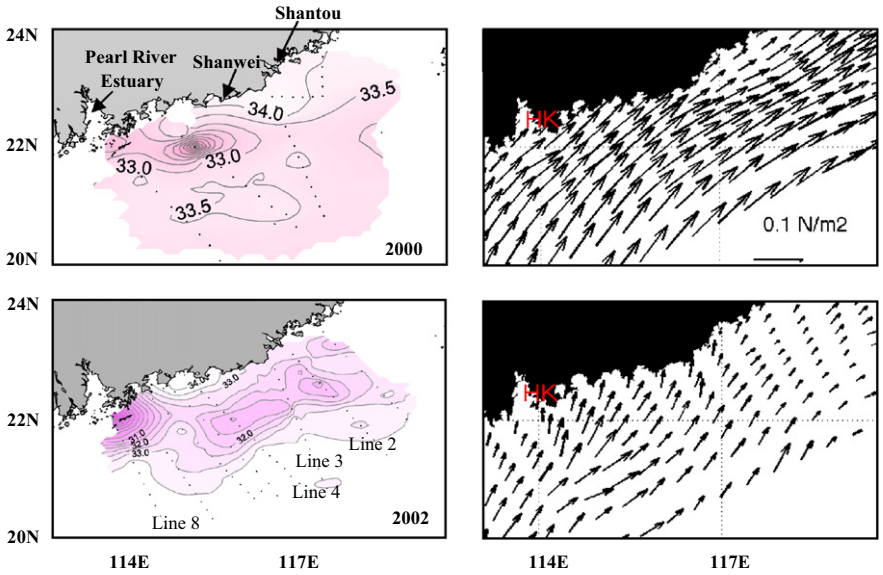

Fig. 3. Salinity (psu) at 5 m (left panels) and corresponding QuickScat surface wind stress vectors (Pa) during the summer in 2000 (July 19–August 2, upper panel on the right) and in 2002 (July 22–August 1, lower panel on the right). The respective Pearl River volume discharge rates were 10,300 $m^3 s^{-1}$ and 16,100 $m^3 s^{-1}$ for the two time periods.

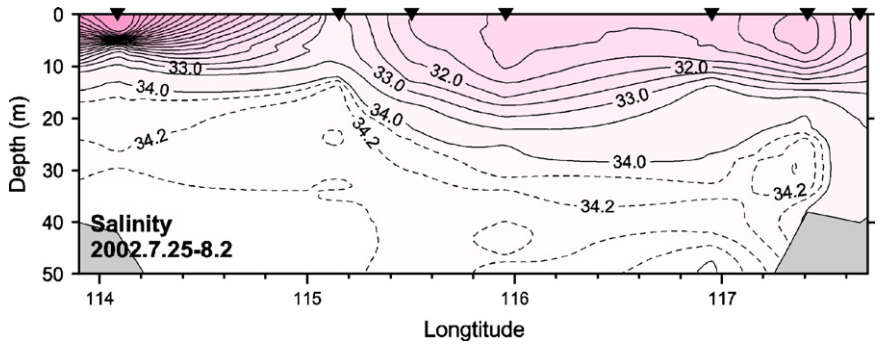

Fig. 4. Salinity as both a function of distance along the central axis of the plume and of water depth from July 25 to August 2, 2002.

As in 2000, the plume was patchy, with the lowest SSS centers distributed along the central axis of the plume from the PRE toward 118°E. One of the mechanisms that forms the patchy structure in the plume is later shown to result from strong pulses in the river discharge during the 2002 cruise (see below). The plume reached its most southern position near 115°E before heading northeastward. Relatively high SSS was observed in the nearshore water off Shanwei in 2002 rather than off Shantou in 2000. Gan et al. (2007) found that the shoreward transport was markedly intensified near Shanwei owing to both the strengthening bottom Ekman transport over the converging isobaths and to the shoreward geostrophic transport induced by a westward pressure gradient force over the widened shelf east of Shanwei (Fig. 1). The waters with high salinity from the strong upslope advection off Shanwei were subsequently transported eastward by the upwelling coastal current and outcropped at the lee of the coastal cape off Shantou. Because of the weakened southwesterly wind (current) further east of Shanwei (Fig. 3), most of the upwelled cold deep waters near Shanwei were not advected downstream toward Shanwei but were outcropped in Shanwei in 2002. The stronger upwelling favorable wind over the highly stratified plume water during the sampling period of line 4 presumably led to the plume's being located at the southernmost position (also see Fig. 5). A bulge of low SSS with large horizontal SSS gradient was formed in the source region near the entrance of the PRE (west of 114.5°E), while relatively high salinity gradients existed in northern and southern edges of the plume in the far field.

2.2. The vertical structures of the plume and upwelling circulation

The vertical structure along the plume axis over the shelf is displayed by the vertical section of salinity along the track that links the points of minimum SSS in 2002 (Fig. 4). The buoyant water along the plume vertically extended to about 10 m and formed relatively strong salinity gradients along the plume and at the bottom. This fresher plume water was separated from the far-field region on the east by upward isohalines at 115.2°E. Relatively weak salinity gradients but deeper vertical extent of the plume existed in the far field. The plume was detached from the bottom after exiting the PRE at 114°E in the source region (Fig. 4) and also from the coast east of Hong Kong (Fig. 3).

The plume moved offshore while the isohalines tilted upward and shoreward at depth in the cross-shelf sections along lines 2, 3, 4, and 8 in 2002 (Fig. 5). In general, the plume thickened on its offshore side and formed salinity fronts at its southern edge. A strong halocline existed at the bottom of the plume, separating the buoyant water from the seawater below. A relatively thin and highly stratified plume was observed, however, on the inshore

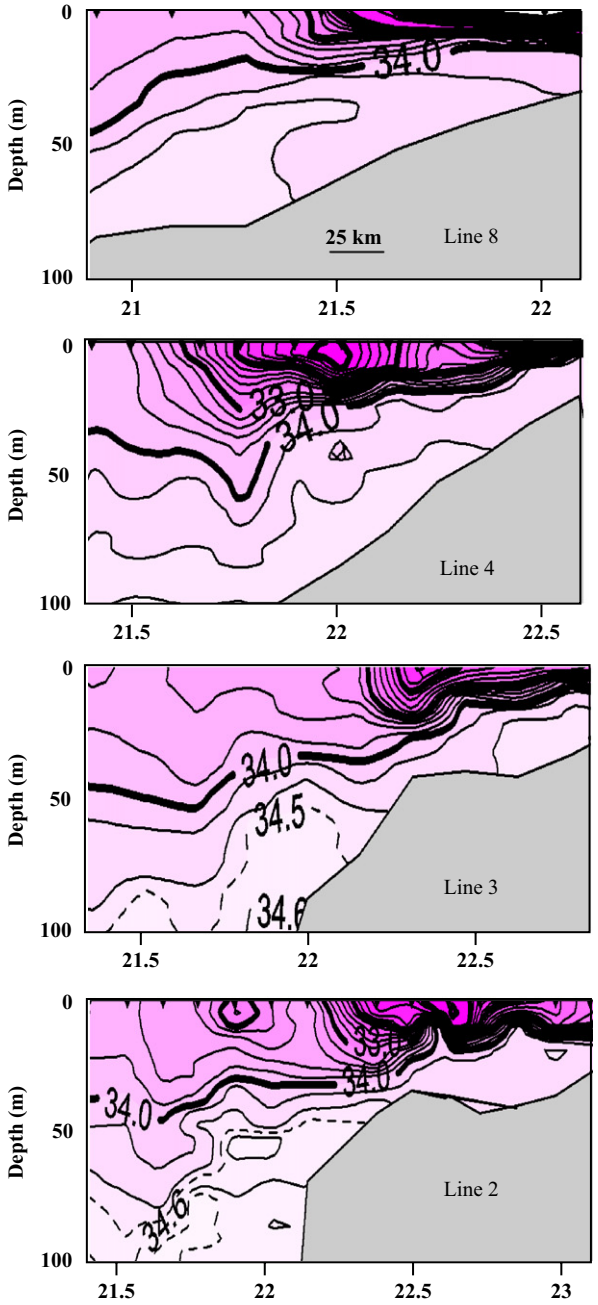

Fig. 5. Cross-shore sections of salinity (psu) along lines 8, 4, 3, and 2 during summer 2002. The contour interval is 0.2 psu. The locations of the sections are marked in Fig. 3.

side of the plume. The thickness difference on the inshore and offshore sides of the plume is probably caused by the formation of respective cyclonic and anticyclonic vorticity because of buoyancy-induced horizontal velocity shear. These characteristics of a wind-driven plume over a shelf were similar to those observed over the shelf near the Delaware Estuary by Munchow and Garvine (1993a, b), except that, in our case, the plume in the NSCS was strongly regulated by coastal upwelling circulation and fully detached from the coast and from the bottom.

Although the hydrographic and remotely sensed data displayed many characteristics of the plume over the shelf of the NSCS during upwelling, many basic processes involved in the interplay between the plume and the upwelling circulation were inevitably unresolved in this spatially and temporally limited data. Conducting process-oriented simulations to establish a comprehensive understanding of basic interactions between the buoyant plume and the wind-driven coastal circulation in the NSCS during summer can compensate for the shortcomings in the data.

3. Modeling study

3.1. The ocean model

For this study, we used the Regional Ocean Model System (ROMS) (Shchepetkin and McWilliams, 2005) for three-dimensional, time-dependent oceanographic flows governed by hydrostatic primitive equations. The vertical mixing parameterization adopted a local closure scheme based on the level-2.5 turbulent kinetic energy equations of Mellor and Yamada (1982). The model domain extended from 15.99°N, 108.17°E in the southwest to about 25.81°N, 119.54°E in the northeast, with its central axis directed 23°N anticlockwise from true east (Fig. 3). A curvilinear grid with a (450, 140) array was adopted as the horizontal mesh (x, y). It corresponded to an average 3 km horizontal grid size. The stretched, generalized, terrain-following s coordinate (Song and Haidvogel, 1994) was adopted as the vertical coordinate. To give higher vertical resolution in the surface and bottom boundary layers, $\theta_s = 2.5$ and $\theta_b = 0.8$ were used in s. The model had thirty vertical levels which formed a minimum grid-spacing of less than 1 m in the water column in the nearshore water and about 10 m over the outer shelf. The water depth, $h(x,y)$, was obtained by merging ETOPO2 (1/30°) from the National Geophysical Data Center (USA) and by digitizing the water depth from navigation charts published by China's Maritime Safety Administration. The minimum water depth was set to 5 m. The topography was smoothed slightly to reduce truncation errors.

To clearly identify the underlying mechanisms of plume-upwelling interaction, these two physical processes were studied as if they were isolated from other forcing processes over the shelf. In this physically motivated simulation, upwelling was assumed to be driven entirely by a spatially uniform southwesterly wind stress (0.025 Pa) which represents typical summer conditions. The model was initialized with horizontally uniform temperature and salinity profiles obtained from the field measurements at station 3A (Fig. 1) which also resembles typical summer climatology in the World Ocean Database 2001 (Boyer et al., 2005). Also based on the field measurements, the salinity and temperature of the river were set to 10 psu and 29.5 °C over the entire water column at the head of the PRE. The velocities and surface elevation were initialized to zero. The model domain had two open boundaries to which open boundary conditions (OBCs) favorable for simulating shelf circulation (Gan and Allen, 2005) were applied. The buoyancy flux from the atmosphere was set to zero for simplicity. A discharge rate for the Pearl River was set to be the 16,500 $m^3 s^{-1}$ which is the average rate from June to August from 1993 to 2004. The model was run for 30 days and daily-averaged outputs were used in the analyses.

3.2. The river plume in upwelling circulation

The general characteristics of the response of coastal water to the southwesterly wind and buoyancy forcing are shown in Fig. 6. The coastal current flows mostly parallel to the coastline west of the PRE, but veers offshore as it encounters the widening isobaths east of Shanwei (Fig. 6a). It bifurcates into northern and southern components near the Taiwan Shoals. The much stronger southern component of the split flow heads southeast following

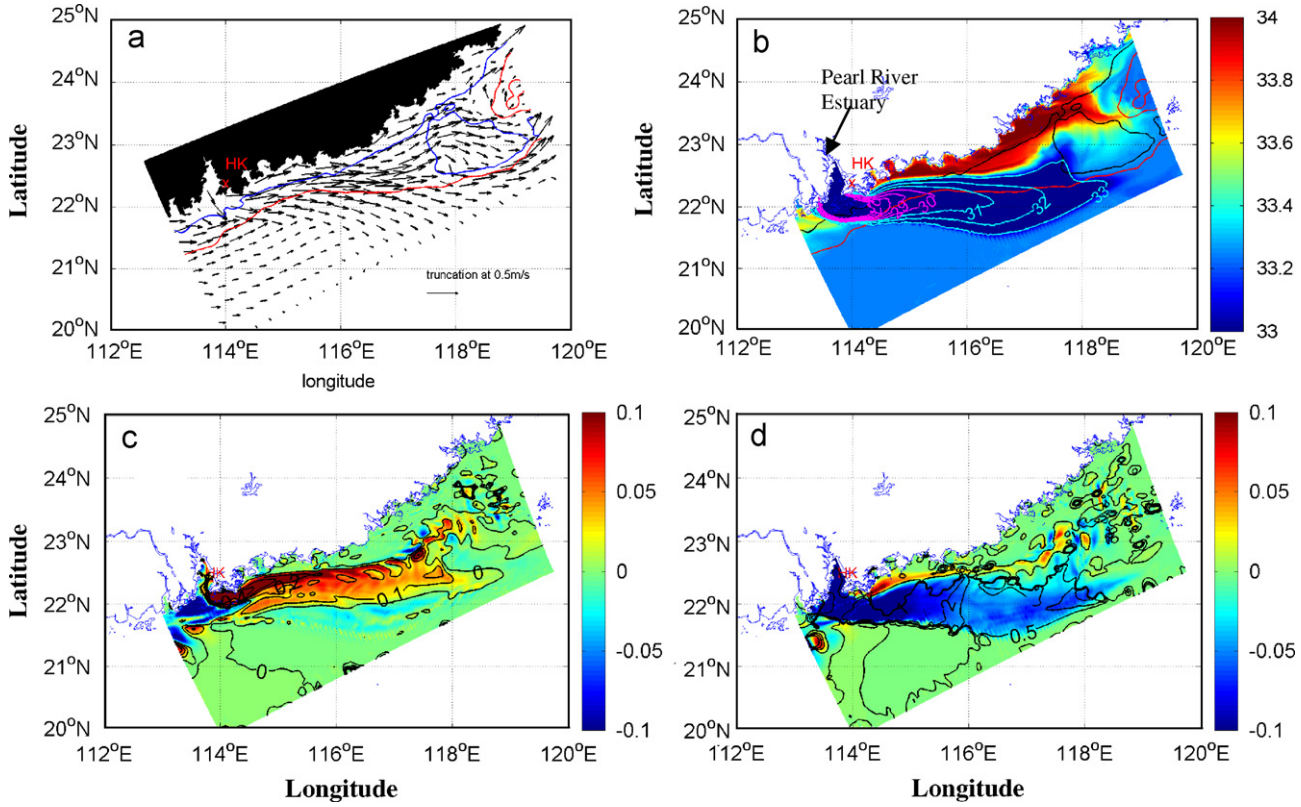

Fig. 6. (a) Surface velocity vectors (ms^{-1}); (b) surface salinity (psu); (c) the differences of surface alongshore velocities (Δu, ms^{-1}); and (d) cross-shore velocities (Δv, ms^{-1}) for the cases with and without the river discharge on day 30. In (c) and (d), the color contours are the differences, and the black contour lines and labeled numbers refer to the percentage change in the respective velocities caused by the buoyant plume.

the local isobaths, while the northern component continues to flow northeastward parallel to the coast.

More specifically Fig. 6b shows that upwelling provided highly saline water to the nearshore and that the saline water extended farther offshore over the wider shelf. Relatively high salinity water also existed in the lee of the coastal cape off Shantou which is similar to what was observed in the 2000 field data shown in Fig. 3. Fig. 6b also shows that the plume water advected eastward with its central axis approximately directed 22.1°N over the shelf. The central axis gradually turned toward the offshore side of the upwelling jet as the plume flowed from the source region. The southward shift of the plume over the shelf is accounted for by surface wind-driven Ekman flow and by pressure gradient force caused by the density gradient at the nose of the plume (to be discussed in Section 4.3). The plume widened as it progressed southeastward and bifurcated near the Taiwan Shoals, similar to the 2002 SSS field shown in Fig. 3. A quasi-stationary freshwater bulge formed at the entrance of the PRE (Fig. 6b), which had SSS$\leqslant$30 psu and is represented by purple contours. Strong horizontal SSS gradients on its outer edge were surrounded by ambient less saline water. The gradients decreased in the plume over the far field.

The less dense plume water and the seawater formed density fronts at the lateral edges of the plume, particularly on its northern flank, where the upwelled dense water over the inner shelf met the lighter plume water offshore. The effects of the buoyant plume on the coastal current can be readily shown by the differences in the property fields resulting from the case with the river discharge subtracting property fields from the case without river discharge (Fig. 6c and d). With the river discharge present, the surface alongshore currents (u) increased more than 30% in the source region and about 10% in the far field in the plume-influenced water. Interestingly, a much larger enhancement was found in the seaward surface velocities (v) over the plume, which increased more than two-fold in the source region and 50–100% over the rest of the plume-influenced shelf. It is later shown that the increase of offshore currents was induced mainly by the plume-strengthened surface Ekman transport and partially by the southward geostrophic currents at the nose of the eastward-propagating plume.

3.3. Plume propagation over the shelf

The propagation of the plume, after detaching from the bottom and the coast, often behaves like a first mode baroclinic wave that results from the density difference between the river and seawater as described by inviscid theory (Chao and Boicourt, 1986; Garvine, 1987; Rennie et al., 1999). Fig. 7a shows that the plume first formed a quasi-stationary bulge after leaving the estuary. As the freshwater bulge grew, its outer part gradually accelerated southeastward at a speed of about 0.07 ms^{-1} in the source region west of 114.5°E and reached a speed of 0.2 ms^{-1} (Fig. 7b). This was the same speed as the wind-driven along-plume current in the far field. These propagation speeds were much smaller than $Ci = 0.54\,ms^{-1}$ which is the phase speed of the linear internal wave. Kourafalou et al. (1996b) and Hickey et al. (1998) also found that plumes were strongly wind-driven over continental shelves. With the rear of the plume advancing slower than its nose as indicated in Fig. 7a, the plume's widening (Fig. 6b) may have resulted more from the surface Ekman drift than from lateral detrainment (Stern et al., 1982).

With a fast moving plume emanating from the slower moving bulge, the Pearl River discharge gradually transported downstream

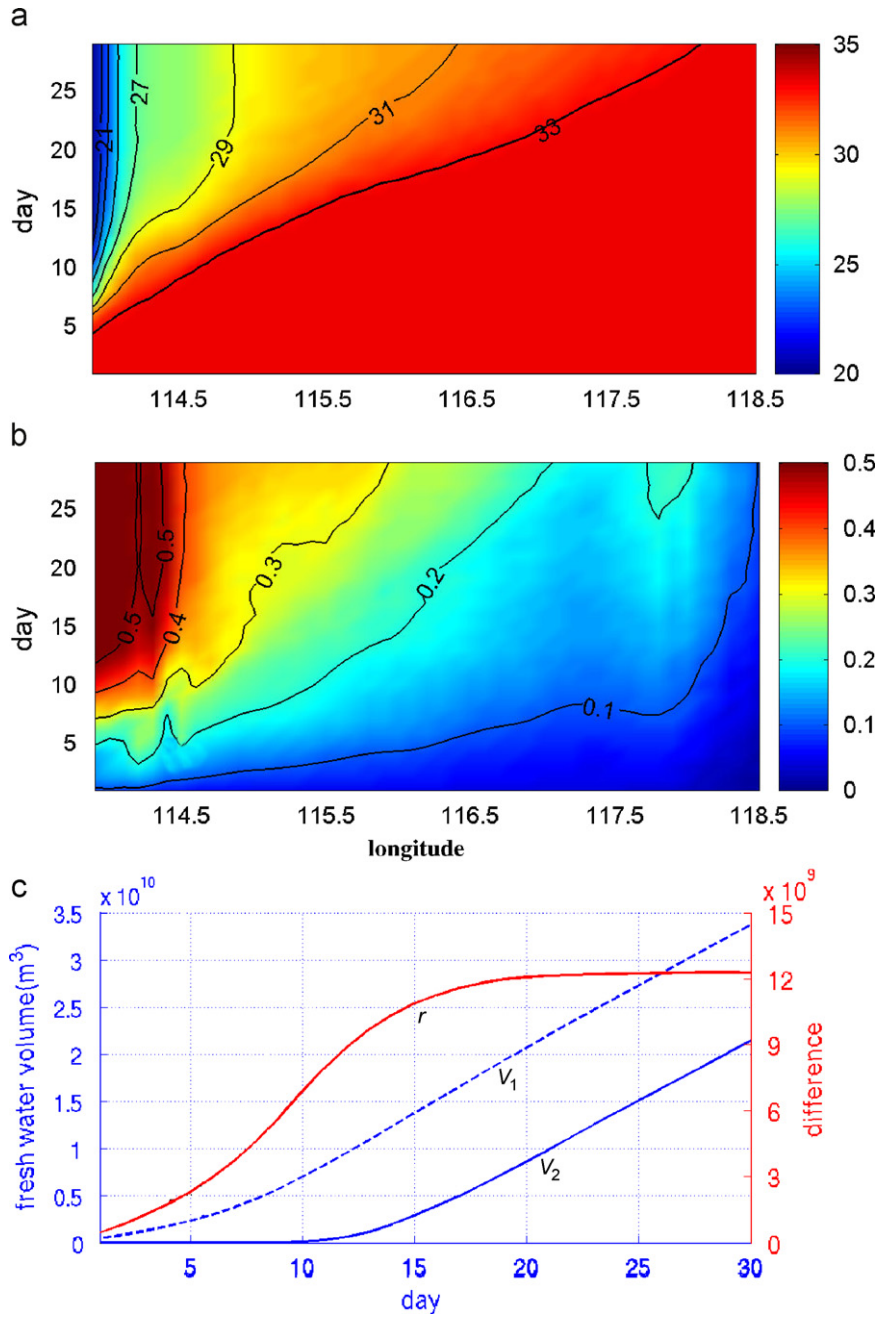

Fig. 7. Time series of (a) surface salinity (psu); (b) along-plume velocity (ms^{-1}) as a function of distance along the axis of the plume (22.1N) and (c) time series of total freshwater volume for the entire domain (dashed blue line), the freshwater volume advected by the coastal current east of 114.5°E (solid blue line), and their difference (red line). (For interpretation of the references to colour in this figure legend, the reader is referred to the web version of this article.)

onto the shelf while the buoyant water accumulated within the bulge. However, after a certain point, this was no longer true. Fig. 7c presents the difference, $\boldsymbol{r}$, of the total volume discharge water (V_1) from the volume advected to the shelf east of 114.5°E (V_2) according to

$$V_1 = \int_V \frac{S_{sea} - S_p}{S_{sea}}\, dV \tag{1}$$

$$V_2 = \int_{V_{114.5}} \frac{S_{sea} - S_p}{S_{sea}}\, dV_{114.5} \tag{2}$$

where S_{sea} ($=33.3$ psu) and S_p ($\leqslant 33$ psu) are the salinities of the seawater and the plume, respectively. V is the total volume of the model domain and $V_{114.5}$ is the volume occupied by the region east of 114.5°E. Time series of V_1, V_2, and $\boldsymbol{r}$ are presented in Fig. 7c. After exiting the bulge, it took 10 days for the lighter plume water to reach 114.5°E. Afterwards, V_1, and V_2 increased linearly with time and $\boldsymbol{r}$ reached a steady state by day 20. There was no further plume water accumulation in the bulge by day 20 and all newly discharged freshwater advected downstream. Since the river discharge rate was steady, it would be the same as saying that the volume of the downstream freshwater transport matched the freshwater source by day 20. The result here indicates that the coastal current was close enough to the bulge at the entrance of the PRE that it limited the growth of the bulge. An unsteady state could be expected if the ambient coastal current did not extend to the bulge (Chant et al., 2008).

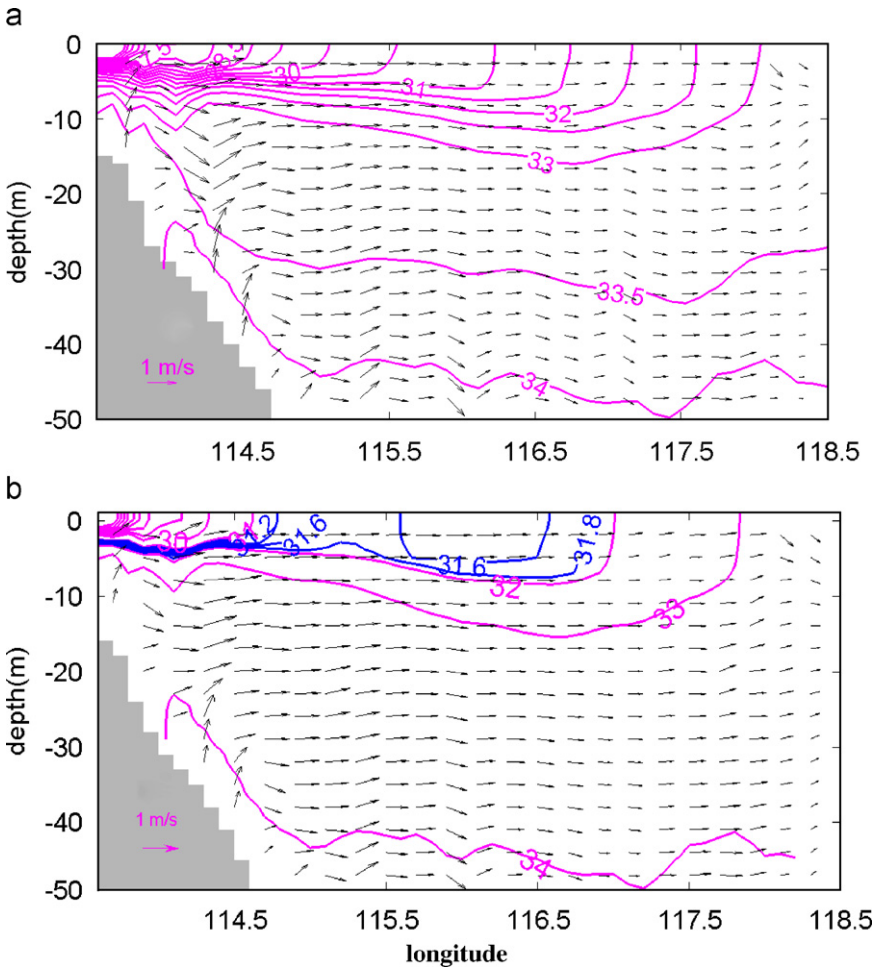

Fig. 8. Salinity (psu) and velocity vectors (ms^{-1}) as functions of both depth and distance along the axis of the plume (22.1°N) on day 30 for cases forced (a) by a steady river discharge rate of 16,500 $m^3 s^{-1}$ and (b) by a pulse-like river discharge rate, in which the southeastward propagating plume is interrupted by upward isohalines. The vertical velocity is scaled by 5×10^3 ms^{-1}.

3.4. Along-plume structure

Fig. 8a shows a vertical section of salinity as a function of depth and distance along the plume's axis. The plume extended vertically from about 10 m in the source region to 15 m in the far field. Stratification decreased towards the nose of plume which is qualitatively similar to the observations presented in Fig. 4. However, the observed upward isohaline near 115°E is absent in the simulated field of Fig. 8a. An additional experiment was run in which the unsteady river discharge rate was linearly increased from 0.6×10^4 to 1.6×10^4 $m^3 s^{-1}$ within the first 10 days. Then it was decreased to the minimum value again on day 20 followed by the peak value again on day 30. Unlike forcing with a steady river discharge rate, the isohaline did move upward near 115.5°E as seen in Fig. 8b. The pulse-like plume structure over the shelf can form as a result of an unsteady river discharge and the temporal variation of the river discharge can lead to vertical displacement of the pycnocline at the edge of the pulsed plume. Tides, wind, and current variability, of course, could also be the forcing agents for this patchy structure of plume.

Fig. 8 also suggests that the along-plume velocities were strong just east of the source region where the plume was close to the coastal upwelling jet. However, the velocities were relatively weak in the far field because Ekman drift caused the plume to advect away from the jet core. Therefore, the plume does not always flow along the core of the upwelling jet. A near-surface downward motion at the nose of the plume was accompanied by a thicker layer of upward motion beneath it. Relatively strong upward motion was also observed in the simulated upslope currents within the bottom boundary layer.

3.5. Responses of cross-shelf fields

The alongshore variations in the salinity (s) and velocities (u, v) on day 30 along cross-shelf sections near the entrance of the PRE (line 256) and near Shanwei (line 305) are shown in Fig. 9. The transect lines are denoted by their alongshore grid numbers in Fig. 1. The differences in these variables (Δs, Δu and Δv), with and without river discharge present, are also shown. The directions of (u, v) are parallel to and normal to the model's curvilinear coordinate at the southern boundary, respectively, with positive values referring to the northeastward and northwestward directions, respectively. Thus, v approximately represents the cross-shelf velocity. In particular, line 256 is close to line 8, and line 305 near Shanwei is analogous to line 4 in the field surveys shown in Fig. 5.

Fig. 9 shows the typical circulation in the wind-driven cross-shelf upwelling over a plume-influenced shelf. It is characterized by seaward-moving buoyant water in the plume layer and shoreward advection of high salinity (dense) water near the bottom. Under a steady wind, Fig. 9 shows that the plume gradually widened in the seaward direction, thickened from

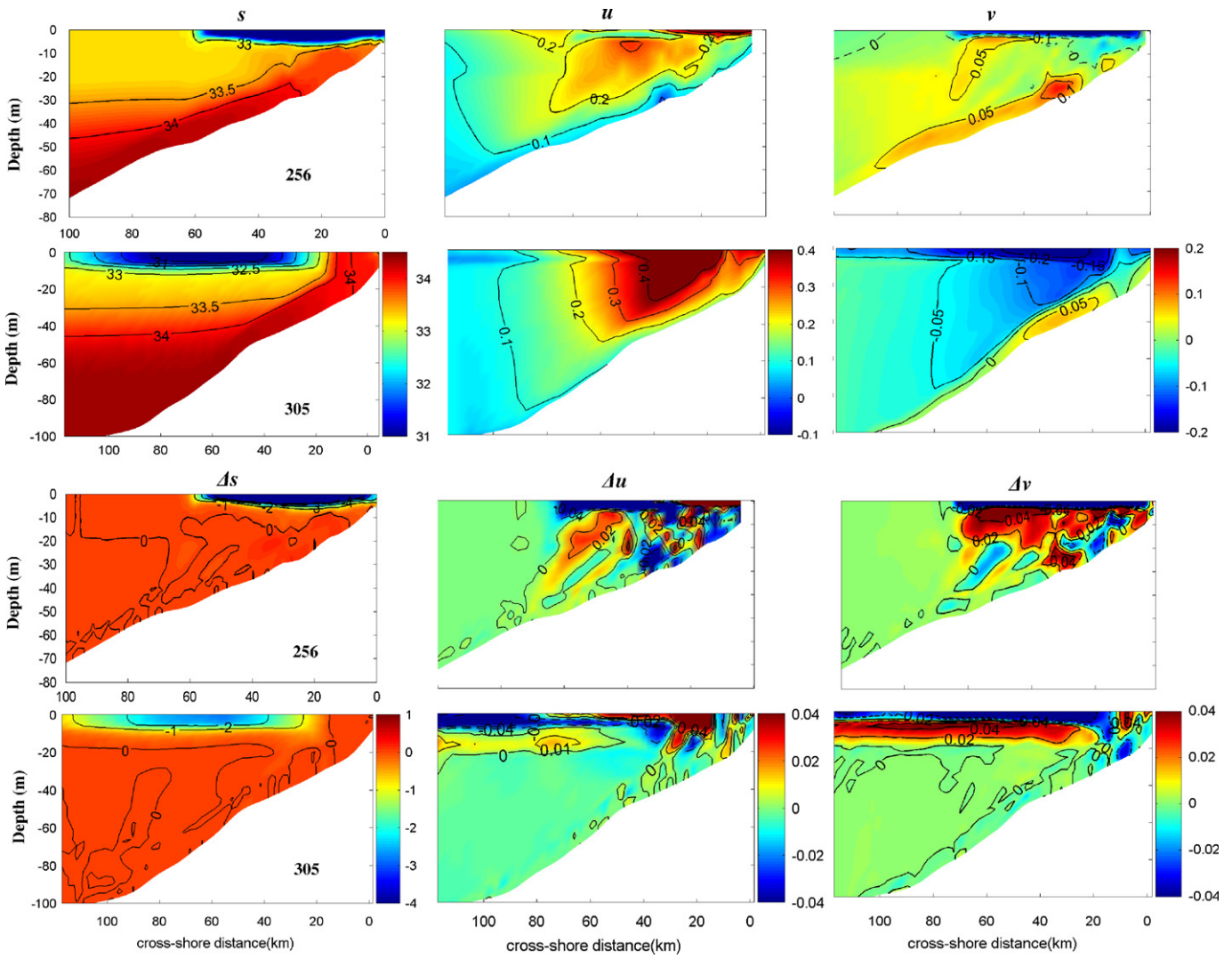

Fig. 9. Across-shore sections of salinity (S, psu), alongshore velocity (u, ms^{-1}), cross-shore velocity (v, ms^{-1}) at line 256 off Hong Kong and line 305 off Shanwei on day 30. The corresponding differences (Δs, Δu, and Δv) between the case with and without river discharge are also shown in the last two rows.

line 256 toward line 305, and detached from the coast near line 305. Meanwhile, a density front with a strong horizontal density gradient formed on the inshore edge of the plume between the upwelled dense water and the plume itself.

Ekman dynamics explains the positioning of the coastal upwelling jet in the northern part of the plume. The geostrophic balance between the plume and ambient seawater accounts for the weakened jet on the plume's offshore edge ($\Delta u<0$) and the strengthened ($\Delta u>0$) jet on the plume's inshore edge within the plume-influenced layer at line 256. Similar conditions also occurred at line 305. While the plume effects on u were mainly in the plume-influenced upper part of the water column at line 305 in the far field, they penetrated into deeper water at line 256 near the source, similar to the findings by Hickey et al. (1998) and Berdeal et al. (2002).

One of the most striking effects of the buoyant plume on the wind-driven current is the great enhancement of offshore transport in the surface layer and the concomitant compensating shoreward current (or weakened offshore transport) beneath it. Obviously, the offshore surface Ekman transport is greatly intensified (large negative Δv) by the increasing wind stress efficiency over the highly stratified upper layer, as pointed out by Lentz (2001) and to be shown in Section 4. The wind stress over the plume enhances the vertical velocity shear stress and, thus, the entrainment between the buoyant upper layer and the layer immediately below it. Nevertheless, the intensification of the cross-shelf circulation in the upper water column has small effects on v in the bottom boundary layer and on the upwelling over the inner shelf. The result implies that the cross-shore quasi-barotropic pressure gradient produced during the wind-driven upwelling over the shelf is not altered by the plume-induced change of cross-shelf transport in the upper water column. This, however, may not be entirely true near the source region because the depth-penetrating nonlinearity induced by the buoyant plume may extend into the deeper layer.

4. Analyses and discussion

The dynamic processes in the plume and coastal circulation can be explained through momentum balances. The depth-dependent momentum

$$\overbrace{\frac{\partial \vec{U}}{\partial t}}^{1} = \overbrace{-2\Omega \times \vec{U}}^{2} \overbrace{-\frac{1}{\rho_0}\nabla P}^{3} + \overbrace{ADV}^{4} + \overbrace{VIS}^{5} \quad (3)$$

where $\vec{U}=(u,v)$ and P is pressure. ρ_0 is the reference density, and Ω is the earth's angular speed of rotation. The terms in (3) are: acceleration, *ACCEL* (term 1); Coriolis force, *COR* (term 2); and the pressure gradient force, *PGF* (term 3). Nonlinear advection, *ADV* (term 4), has horizontal ($HADV=-\vec{U}\bullet\nabla_h\vec{U}$) and vertical ($VADV=-w\bullet(\partial\vec{U}/\partial z)$) components, and the viscous term, *VIS* (term 5), includes horizontal (*HVIS*) and vertical viscous terms (*VVIS*), where w is the vertically upward velocity. We also consider the behavior of the sum of *COR* and *PGF*, which is referred to as the ageostrophic pressure gradient, *AGE*.

$$AGE_{(x,y)}=COR_{(x,y)}+PGF_{(x,y)} \tag{4}$$

AGE is the net difference between the pressure gradient force and the Coriolis force according to (4), so that the sign of $AGE_{(x,y)}$ reflects either the residual Coriolis force or the residual pressure gradient. In the frictional boundary layers, $AGE_{(x,y)}$, generally has the same sign as the Coriolis term and is balanced by the *VVIS*, representing the balances in the Ekman layers.

4.1. Along-plume momentum balance

The momentum balance along the central axis of the plume, x_p ($x_p>0$ directed southeastward, Fig. 10), showed a dominant Ekman balance in the surface and bottom boundary layers while it was mainly geostrophic in the interior. The magnitudes of AGE and VVIS terms in the Ekman balance decreased while the plume was thickening from the source towards the far field. Since the wind stress was spatially uniform, the downstream decrease of the surface Ekman balance was believed to be largely related to the weakening vertical stratification with increasing x_p. As a result, surface offshore velocities ($v_p<0$) decreased, or vorticity $\partial v_p/\partial x_p>0$ occurred along the axis of the plume. This offset the buoyancy-enhanced negative vorticity, $-(\partial u_p/\partial y_p<0)$, at the plume's southern edge, where y_p was normal to the central axis of the plume x_p, but reinforced the local positive vorticity $-(\partial u_p/\partial y_p>0)$, at the plume's northern edge, as shown in Figs. 6c and 9 (and later in Fig. 12). The along-plume momentum generally had very weak nonlinearity where the plume detached from the coast

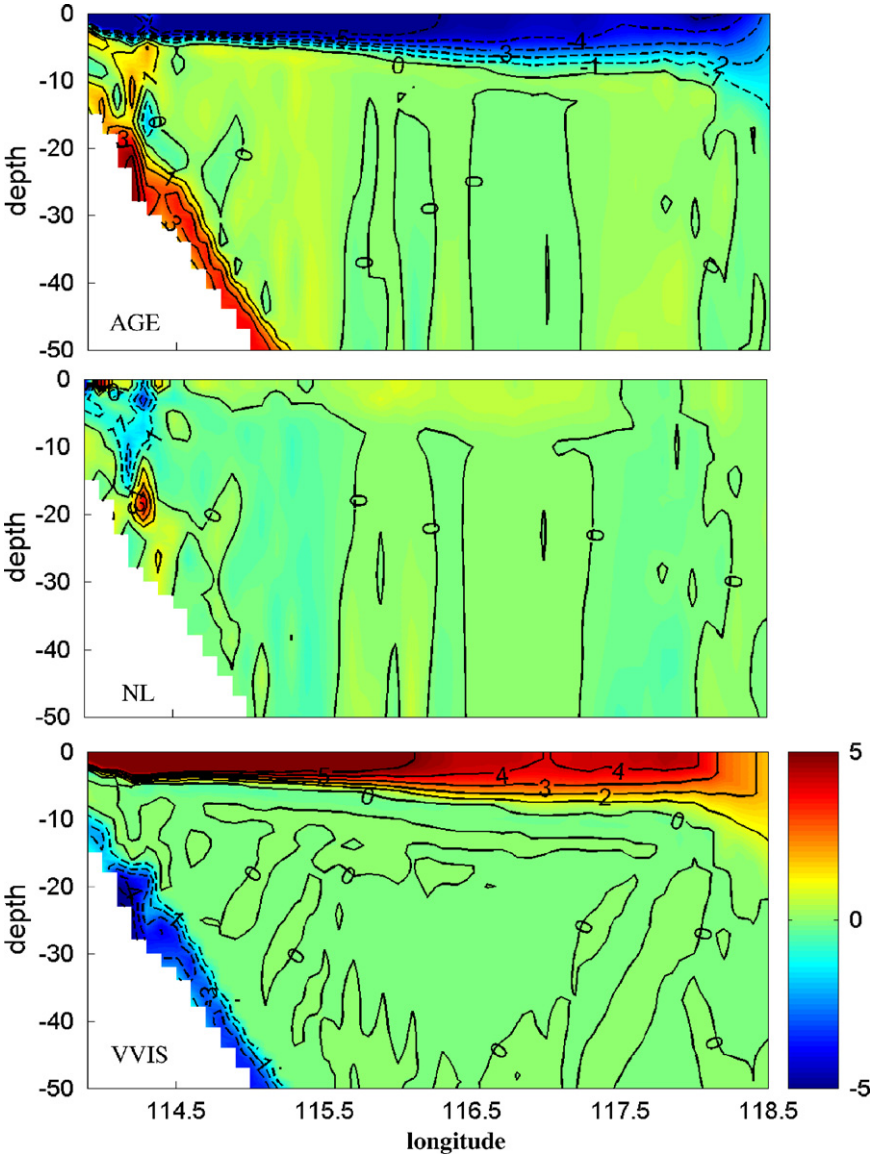

Fig. 10. Terms in the along-plume momentum equation: AGE = ageostrophic pressure gradient; NL = nonlinear advection; and DIFF = vertical viscous term on day 30 ($\times 10^6\,\mathrm{ms}^{-2}$).

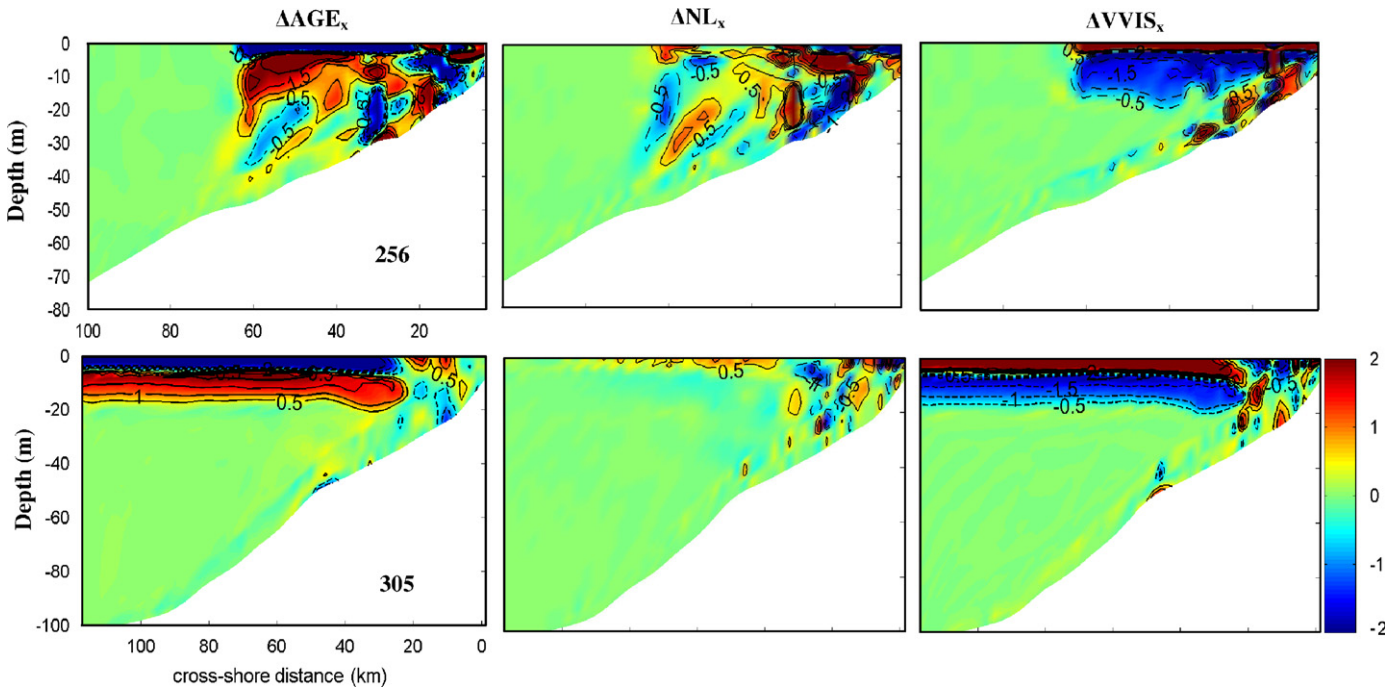

Fig. 11. Cross-shore sections of the differences in the terms of the alongshore momentum equation at lines 256 and 305 on day 30 ($\times 10^6\,\mathrm{ms}^{-2}$): ΔAGE = ageostrophic pressure gradient; ΔNL = nonlinear advection; and ΔDIFF = vertical viscous force.

and the bottom. The nonlinearity became important in the shallower water near the source region as was shown by Munchow and Garvine (1993a, b) as well.

4.2. Plume-influenced cross-shelf momentum balances

The fields of Δu, Δv, and Δs in Fig. 9 were well-correlated with the corresponding balances in Eq. (3) along lines 256 and 305 (shown in Fig. 11). In the alongshore direction (x), at both lines, the stratification of the plume dramatically reduced the surface Ekman depth such that the vertical viscous force weakened ($\Delta VVIS_x < 0$) below the water depth of about 5 m while most of the wind's frictional energy ($\Delta VVIS_x > 0$) was trapped within the plume layer. The $\Delta VVIS_x$ was balanced by ΔAGE_x in Eq. (4) and lead to a negative Δv in the plume layer and a positive Δv in the layer beneath it (Fig. 9). Much stronger ΔNL_x, with a less-organized pattern in the source region, greatly disturbed the flow field at line 256, which was balanced either by $\Delta VVIS_x$ or by ΔAGE_x. In the cross-shore direction (y, not shown), the change of *AGE* term was small in the plume layer, suggesting that the positive and negative Δu on the northern and southern edges of the plume (Fig. 9) arose geostrophically from a pressure gradient induced by the cross-plume density gradient. In both the x and y directions, the buoyancy of the plume had very small effect on the balances in the bottom boundary layer, particularly in the far field region at line 305.

4.3. Plume-alternated cross-isobath transport

The effects of the buoyancy of the plume on the cross-shelf transport during upwelling can be extracted by taking the differences of cross-isobath transport between the cases occurring with and without the presence of river discharge (Fig. 12). The associated dynamic forcing can be obtained from the concurrent along-isobath momentum balances. The 30 and 50 m isobaths were chosen to represent the conditions over the inner shelf (Lentz, 2001; Austin and Lentz, 2002) and over the mid-shelf, respectively, based on the conditions illustrated in Fig. 9.

Because of the nature of wind-driven cross-shelf circulation, the transport in the water column was divided into the upper (M_U) and bottom (M_B) layers where the upper layer was defined as 10 m from the surface and the bottom layer was defined as being 10 m from the bottom. Despite some variations, M_U and M_B represented the transport in the surface and bottom boundary layers reasonably well (Fig. 9). The transport in the middle layer (M_M) was obtained in the interior away from the boundary layers. Positive and negative transport referred to shoreward and seaward transport normal to an isobath, respectively. The mass transport normal to an isobath y^* per unit meter was obtained by

$$M_{y^*} = \int_{h_1}^{h_2} (v_0 \cos\theta - u_0 \sin\theta) dz, \tag{5}$$

where (u_0, v_0) are the eastward and northward currents, respectively, and θ is the angle between the tangent to the isobath and true east. h_1 and h_2 are the depths at the top and bottom of the integrated layer. The transport differences between the cases with and without the presence of river discharge, $\Delta M_{(U, M,B),}$ are shown in Fig. 12.

Besides the features already described, the results show that changes in the transport caused by the plume had a strong along-isobath variation because of the altered balances among the changes in COR_{x^*}, PRE_{x^*}, and $VVIS_{x^*}$ in Eq. (3) (Fig. 12), where x^* is directed along the isobaths with positive values directed eastward. ΔPRE_{x^*} was formed mainly by the horizontal density gradient due to the spatial orientation of the plume. A strong increase in seaward transport in the upper layer coincided with the density minimum along the 30 m isobath (Fig. 13), however, it appeared on the eastern side of the density minimum along the 50 m isobath. The corresponding change in shoreward flows in the middle layer was spatially coherent with the flows in the upper layer, suggesting that the shoreward flow was mainly a compensating one.

These changes in the cross-isobath transport are dynamically reflected in the corresponding momentum balances represented in Fig. 12. In the upper layer, along both isobaths, the enhancement of

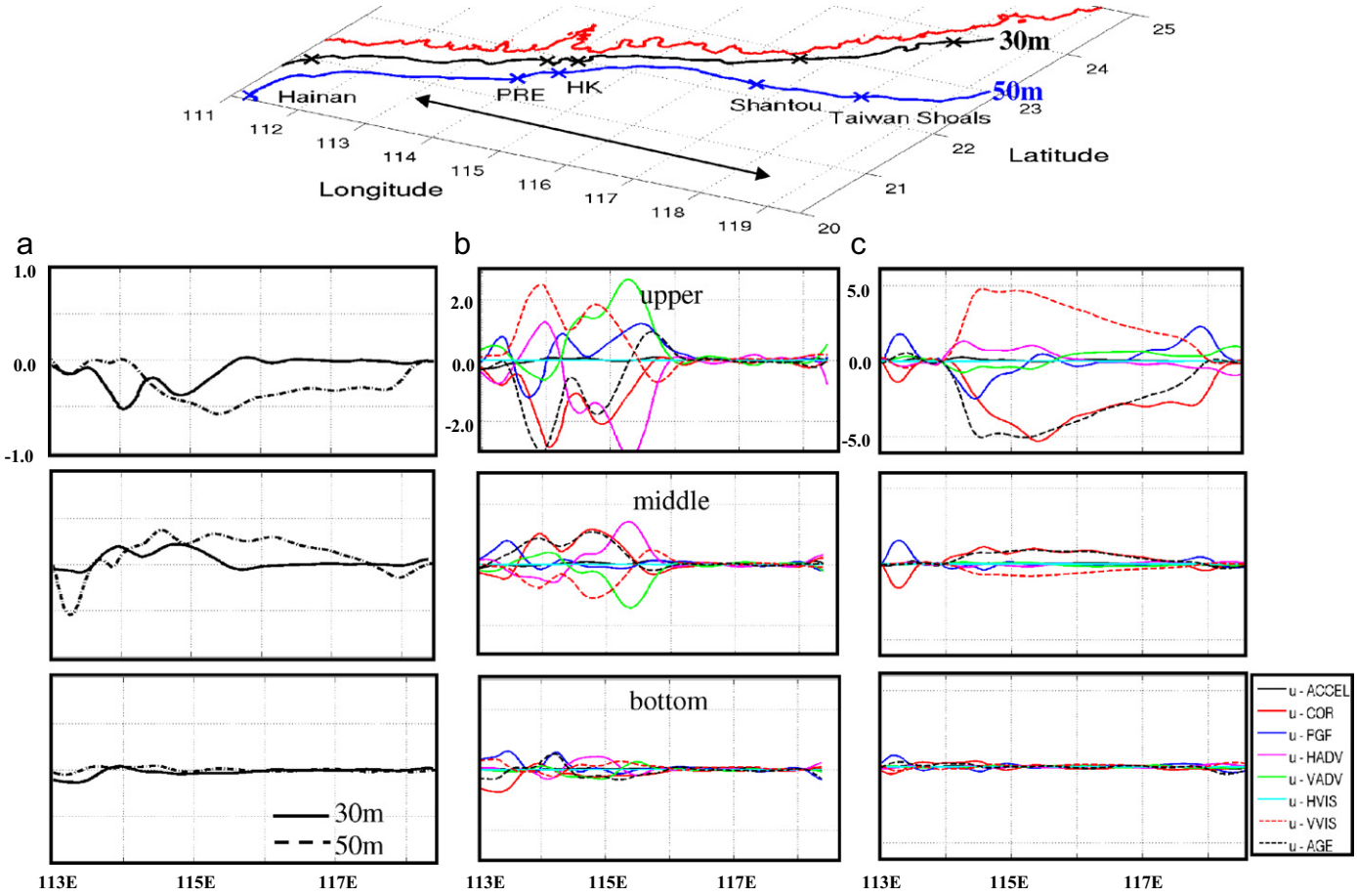

Fig. 12. (a) Differences in daily averaged mass flux (m^2s^{-1}) normal to the 30 m isobath (solid line) and the 50 m isobath (dashed line) with and without river discharge on day 30. They are depth-integrated for the upper 10 m (upper layer); middle 10 m at a depth of 30 m, 30 m at a depth of 50 m (middle layer); and for the bottom 10 m (bottom layer). Positive values of transport are directed shoreward. (b) Differences in daily averaged terms in the momentum equations along the 30 m (central column) on day 30. (c) Same as (b), but along the 50 m isobath. They are depth-integrated in the upper layer (first row), middle layer (second row), and bottom layer (third row); units are ms^{-2}, multiplied by 10^6. ACCEL = acceleration; COR = Coriolis force; PGF = pressure gradient force; HADV = horizontal nonlinear advection; VADV = vertical nonlinear advection; HVIS = horizontal viscous force; VVIS = vertical viscous force; and AGE = ageostrophic term.

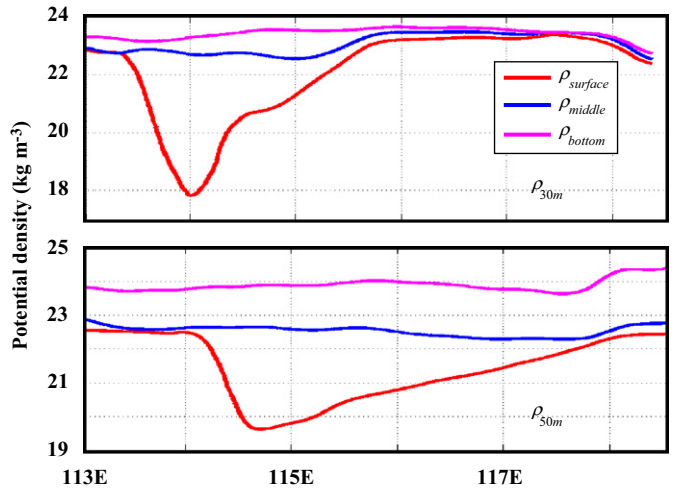

Fig. 13. Depth-averaged potential density (kgm^{-3}) in the upper, middle, and bottom layers along the 30 and 50 m isobaths on day 30.

$VVIS_{x^*}$ ($\Delta VVIS_{x^*}>0$) was mainly balanced by the ΔAGE_{x^*} which was the ΔCOR_{x^*} residual after deducting the contributions from ΔPGF_{x^*}. Thus, the dominant balance was among $\Delta VVIS_{x^*}$, ΔCOR_x, and ΔPGF_{x^*}, while $\Delta HADV_{x^*}$ and $\Delta VADV_{x^*}$ balanced each other. A distinct ΔPGF_{x^*} dipole with negative/positive value on the western/eastern side of the plume were centered at 114°E along the 30 m isobath and at 115.3°E along the 50 m isobath. Since $\Delta PGF_{x^*}<0$ is geostrophically unfavorable (and $\Delta PGF_{x^*}>0$ is favorable) for seaward transport in the upper layer, this dipole ΔPGF_{x^*} increased/decreased offshore transports on western/eastern side of the plume along the isobaths. The $\Delta VVIS_x$, on the other hand, was controlled by the strength of vertical stratification and generally decreased downstream. Thus, $\Delta VVIS_x$ and ΔPGF_{x^*} jointly controlled the plume-induced cross-shore transport. Along the 30 m isobath, the maximum ΔM_U was located at 114°E where $\Delta VVIS_{x^*}$ $+\Delta PGF_{x^*}=\Delta COR_{x^*}$ was at a maximum, coinciding with the $\Delta VVIS_{x^*}$ maximum and density minimum. Along the 50 m isobath, due to the existence of the negative ΔPGF_{x^*} maximum where positive $\Delta VVIS_x$ was greatest, the offshore transport maximum diverted from the density minimum and the $\Delta VVIS_{x^*}$ maximum and occurred east of them. It is also obvious that the positive ΔPGF_{x^*} existed at the nose (118°E) of the plume along the 50 m isobath, which geostrophically increased the offshore transport and contributed to the offshore shifting of the plume, as shown in Section 3.2. The balance between $\Delta HADV_{x^*}$ and $\Delta VADV_{x^*}$ in the upper layer along both the 30 and 50 m isobaths implies a strong downward advection of southeastward horizontal momentum existed in the source region and a much weaker upward advection

existed offshore. Symmetric but opposite responses to the changes in the along-isobath momentum balance occurred in the middle layer, while the change was negligible in the deep layer.

5. Conclusions

Observations and modeling studies demonstrated the interactive processes between a river plume and upwelling circulation and identified the associated forcing mechanisms over the continental shelf in the NSCS. The results suggest that the river plume from the PRE is shaped largely by the prevailing wind-driven coastal circulation over the shelf in the NSCS. The buoyancy in the plume, in turn, considerably modulates the alongshore and cross-shelf upwelling circulation in the upper water column.

After leaving the PRE, the plume typically forms a slowly expanding plume bulge near the estuary's mouth in which river water in the outer part of the bulge is constantly advected southeastward by wind-driven upwelling coastal current. It forms a widening and thickening plume over the shelf. The freshwater accumulation in the bulge at the estuary's mouth increases with time until the bulge reaches the shelf where all newly discharged freshwater is carried downstream. Temporal variation in the river's discharge rate is one of the possible mechanisms that leads to the formation of a pulse-like plume structure.

The buoyancy in the plume alters the wind-driven upwelling circulation by thinning and strengthening both the seaward transport in the plume and the shoreward transport beneath it. However, it has little effect on the water column below 20 m and, thus, on the intensity of the upwelling. Lateral pressure gradients from the buoyancy difference between the plume and the ambient seawater geostrophically enhance the intensity of the current along the inshore edge but weaken it on the offshore edge of the plume, and the along-plume weakening of stratification decreases the surface offshore current downstream. A highly nonlinear response near the source region enhances the vertical advection of horizontal momentum in the upper layer, while the flow is mainly geostrophic and the vertical advection of horizontal momentum is weaker in the far field. The spatial distribution of the plume over the shelf leads to alongshore variations in the cross-shore transport in the upper water column by alternating Ekman dynamics in the surface layer and by forming an along-isobath pressure gradient. A shelf regions that has interactive plume-current processes behaves differently from those without, which is important not only to physical processes in the coastal ocean, but also to the biogeochemical processes.

Acknowledgements

This research was supported by the Hong Kong's Research Grants Council under grants CERG-601105 and CERG-601008, and NSFC-RGC project (Grant No. 40731160624 and N_HKUST623/07), by the National Key Basic Research Development Program 2009CB421208 to Gan and 2009CB421205 to Li and Guo and by NSFC project (Grant No. 40576013) to Wang. The authors greatly appreciate the help provided by L. Liang, Y. Cheung, and T. Zu for processing the data. The authors also thank the two anonymous reviewers for their valuable suggestions.

References

Allen, J.S., Newberger, P.A., Federiuk, J., 1995. Upwelling circulation on the Oregon continental shelf. Part 1: response to idealized forcing. J. Phys. Oceanogr. 25, 1843–1866.

Austin, J.A., Lentz, S., 2002. The inner shelf response to wind-driven upwelling and downwelling. J. Phys. Oceanogr. 32, 2171–2193.

Berdeal, B., Hickey, I.B.M., Kawase, M., 2002. Influence of wind stress and ambient flow on high discharge river plume. J. Geophys. Res. 107 (C9), 3130.

Boyer, T.P., Levitus, S., Antonov, J.I., Locarnini, R.A., Garcia, H.E., 2005. Linear trends in salinity for the World Ocean, 1955–1998. Geophys. Res. Lett. 32, L01604, doi:10.1029/2004GL021791.

Chant, R.J., Glenn, S.M., Hunter, E., Kohut, J., Chen, R.F., Houghton, R.W., Bosch, J., Schofield, O., 2008. Bulge formation of a buoyant river outflow. J. Geophys. Res. 113, C01017.

Chao, S.Y., 1988. Wind-driven motion of estuarine plumes. J. Phys. Oceanogr. 18, 1144–1166.

Chao, S.Y., Boicourt, W.C., 1986. Onset of an estuarine plume. J. Phys. Oceanogr. 16, 2137–2149.

Chen, C., Xue, P., Ding, P., Beardsley, R.C., Xu, Q., Mao, X., Gao, G., Qi, J., Li, C., Lin, H., Cowles, G., Shi, M., 2008. Physical mechanisms for the offshore detachment of the Changjiang diluted water in the East China Sea. J. Geophys. Res. 113, C02002.

Dong, L.J., Su, L.A., Wong, Z., Cao, Chen, J., 2004. Seasonal variation and dynamics of Pearl River plume. Continental Shelf Research 24, 1761–1777.

Fong, D., Geyer, W.R., 2002. The alongshore transport of freshwater in a surface-trapped river plume. J. Phys. Oceanogr. 32, 957–972.

Gan, J., Allen, J.S., 2002. A modeling study of shelf circulation off northern California in the region of the coastal ocean dynamics experiment, response to relaxation of upwelling. J. Geophys. Res. 107 (C9), 3123.

Gan, J.P., Allen, J.S., 2005. On open boundary conditions in a limited-area coastal model off Oregon Part 1: response to idealized wind forcing. Ocean Modeling 8, 113–115.

Gan, J.P., Cheung, Y.Y., Guo, X., Li, L., 2007. Upwelling intensification over a widened shelf in the northeastern South China Sea. J. Geophys. Res. 9 (submitted).

Garvine, R.W., 1987. Estuary plumes and fronts in shelf waters: a layer model. J. Phys. Oceanogr. 17, 1877–1896.

Hickey, B.M., Thomson, R.E., Yih, H., LeBlond, P.H., 1991. Velocity and temperature fluctuations in a buoyancy-driven current of Vancouver Island. J. Geophys. Res. 96, 10,507–10,538.

Hickey, B.M., Pietrafesa, L.J., Jay, D.A., Boicourt, W.C., 1998. The Columbia river plume study: subtidal variability in the velocity and salinity fields. J. Geophys. Res. 103, 10,339–10,368.

Kourafalou, V.H., Oey, L., Wang, J.D., Lee, T.L., 1996a. The fate of river discharge on the continental shelf 1. Modeling the river plume and the inner shelf coastal current. J. Geophys. Res. 101, 3415–3434.

Kourafalou, V.H., Lee, T.L., Oey, L., Wang, J.D., 1996b. The fate of river discharge on the continental shelf 2. Transport of coastal low-salinity waters under realistic wind and tidal forcing. J. Geophys. Res. 101, 3435–3455.

Lentz, S.J., 2001. The influence of stratification on the wind-driven cross-shelf circulation over the north Carolina shelf. J. Phys. Oceanogr. 23, 2749–2760.

Li, L., 1993. Summer upwelling system over the northern continental shelf of the South China Sea: a physical description. In: Su, J., Chuang, W.-S., Hsueh, R.Y. (Eds.), Proceedings of the Symposium on the Physical and Chemical Oceanography of the China Seas. China Ocean Press, Beijing, pp. 58–68.

Mellor, G.L., Yamada, T., 1982. Development of a turbulence closure model for geophysical fluid problems. Rev. Geophys. 20, 851–875.

Munchow, A., Garvine, R.W., 1993a. Dynamical properties of a buoyancy-driven coastal current. J. Geophys. Res. 98, 20,063–20,077.

Munchow, A., Garvine, R.W., 1993b. Buoyancy and wind forcing of a coastal current. J. Mar. Res. 51, 293–322.

Nash, J., Moum, J.N., 2005. River plume as a source of large-amplitude internal waves in the coastal ocean. Nature 437.

Oey, L.Y., Mellor, G.L., 1993. Subtidal variability of estuarine outflow, plume, and coastal current: a model study. J. Phys. Oceanogr. 23, 164–171.

Rennie, S.E., Largier, J.L., Lentz, S.J., 1999. Observations of a pulsed buoyancy current downstream of Chesapeake Bay. J. Geophys. Res. 104, 18,227–18,240.

Shaw, P.T., 1992. Self circulation off the southeast coast of China. Rev. Aquat. Sci. 6 (1), 1–28.

Shchepetkin, A.F., McWilliams, J.C., 2005. The regional ocean modeling system: a split-explicit, free-surface, topography-following coordinates ocean model. Ocean Modeling 9, 347–404.

Song, Y.T., Haidvogel, D., 1994. A semi-implicit ocean circulation model using a generalized topography following coordinate system. J. Comp. Phys. 115, 228–248.

Stern, M.E., Whitehead, J.A., Hua, B.L., 1982. The intrusion of a density current along the coast of a rotating fluid. J. Fluid Mech. 123, 237–265.

Su, J., 1998. Circulation dynamics of the China seas north of 18°N. In: Allan, R.R., Kenneth, H., Brink (Eds.), The Sea, Vol. 11, The Global Coastal Ocean: Regional Studies and Syntheses. Wiley, NY, pp. 483–505.

Whitney, M.M., Garvine, R.W., 2005. Wind influence on a coastal buoyant outflow. J. Geophys. Res. 110, C03014.

Wong, L., Chen, J., Dong, L., 2004. A model of the plume front of the Pearl River Estuary, China and adjacent waters in the winter dry season. Continental Shelf Research 24, 1779–1795.

Xu, J., Guo, X., Li, L., Wu, R., Jing, C., 2003. Hydrology features in outer sea of eastern Guangdong in summer 2002. J. Oceanogr. Taiwan Strait 22 (2), 269–277 (in Chinese).

Yankovsky, A.B., Chapman, D.C., 1997. A simple theory for the fate of buoyant coastal discharges. J. Phys. Oceanogr. 27, 1386–1401.

Yankovsky, A., Hickey, B.M., Munchow, A.K., 2001. Impact of variable inflow on the dynamics of a coastal buoyant plume. J. Geophys. Res. 106, 19,809–19,824.

Zhuang, W., Wang, D., Wu, R., Hu, J., 2005. Coastal upwelling off eastern Fujian, Guangdong detected by Remote Sensing. Chin. Atmos. Sci. 29 (3), 438–443 (in Chinese).